Astronomy & Astrophysics manuscript no. coma_Virtis_submitted_referee ©ESO 2015
May 19, 2015

First observations of H_2O and CO_2 vapour in comet 67P/Churyumov-Gerasimenko by VIRTIS onboard Rosetta

D. Bockelée-Morvan[1], V. Debout[1], S. Erard[1], C. Leyrat[1], F. Capaccioni[2], G. Filacchione[2], N. Fougere[3], P. Drossart[1], G. Arnold[4], M. Combi[3], B. Schmitt[5], J. Crovisier[1], M.-C. de Sanctis[2], T. Encrenaz[1], E. Kürt[4], E. Palomba[2], F.W. Taylor[6], F. Tosi[2], G. Piccioni[2], U. Fink[7], G. Tozzi[8], A. Barucci[1], N. Biver[1], M.-T. Capria[2], M. Combes[1], W. Ip[9], M. Blecka[10], F. Henry[1], S. Jacquinod[1], J.-M. Reess[1], A. Semery[1], and D. Tiphene[1]

[1] LESIA, Observatoire de Paris, LESIA/CNRS, UPMC, Université Paris-Diderot, F-92195 Meudon, France
e-mail: dominique.bockelee@obspm.fr

[2] INAF-IAPS, Istituto di Astrofisica e Planetologia Spaziali, via del fosso del Cavaliere, 100, 00133, Rome, Italy

[3] Space Physics Research Laboratory, University of Michigan, Ann Harbor, MI 48109, USA

[4] Institute for Planetary Research, Deutsches Zentrum für Luft- und Raumfahrt (DLR), Berlin, Germany

[5] Université Grenoble Alpes, CNRS, Institut de Planétologie et d'Astrophysique de Grenoble, Grenoble, France

[6] Department of Physics, Oxford University, Oxford OX1 3PU, UK

[7] Lunar Planetary Laboratory, University of Arizona, Tucson, USA

[8] INAF, Osservatorio Astrofisico di Arcetri, Largo E. Fermi 5, 50125 Firenze, Italy

[9] National Central University, Taipei, Taiwan

[10] Polish Academy of Sciences, Warsaw, Poland

Submitted 00/00/14

ABSTRACT

Context. The understanding of cometary activity is one of the main goals of the Rosetta mission.

Aims. The productions and distributions of water, carbon dioxide and carbon monoxide, which are key species of cometary ices and have different volatility, need to be quantified.

Methods. Using the high spectral-resolution channel of the Visible InfraRed Thermal Imaging Spectrometer (VIRTIS-H), we observed the ν_3 vibrational bands of H_2O and CO_2 at 2.67 and 4.27

μm, respectively, from 24 November 2014 to 24 January 2015, when comet 67P/Churyumov-Gerasimenko was between 2.91 and 2.47 AU from the Sun. Observations were undertaken in limb viewing geometry at distances from the surface of 0 to 1.5 km and with various line-of-sight (LOS) orientations in the body-fixed frame. A geometry tool is used to characterize the position of the LOS with respect to geomorphologic regions and the illumination properties of these regions.

Results. High water column densities are observed for LOS above neck regions, suggesting they are the most productive in water vapour. Whereas water production is weak from regions with low solar illumination, CO_2 is outgassing from both illuminated and non-illuminated regions at about the same rate, which indicates that CO_2 sublimates at a depth that is below the diurnal skin depth. The CO_2/H_2O column density ratio varies from 2 to 30%. For regions into sunlight, mean values between 3 and 6% are measured, with the lowest value for regions Seth and Anuket situated in the most central parts of the body and head of the comet, respectively. The lower bound value is likely representative of the CO_2/H_2O production rate ratio from the neck regions. As for carbon monoxide, we derive column density ratios $CO/H_2O < 1.9$ % and $CO/CO_2 < 80$%. An illumination driven model, with a uniformly active surface releasing water at a mean rate of 7.7×10^{25} s^{-1}, provides an overall agreement to VIRTIS-H data, though some mismatches are witnessing the presence of local surface inhomogeneities in water production. Rotational temperatures of 90–100 K are derived from H_2O and CO_2 averaged spectra.

Key words. Comets: general; Comets: individual: 67P/Churyumov-Gerasimenko; Infrared: planetary systems

Use \titlerunning to supply a shorter title and/or \authorrunning to supply a shorter list of authors.

1. Introduction

Comets are among the most pristine bodies of the solar system and, as such, are expected to provide clues to its chemical and physical properties, 4.6 Gyr ago. More than two dozen molecular species are now identified in cometary atmospheres, pointing to an interstellar-like chemistry (Bockelée-Morvan et al. 2000, 2004). However, questions arise on the extent to which relative abundances measured in cometary atmospheres can be used to constrain chemical models of star-forming regions and proto-planetary disks, since they may not be representative of the nucleus' initial composition. Indeed, outgassing from cometary nuclei involves complex surface and subsurface processes that depend on the physico-chemical properties of the cometary material and ice structure, as well as on current and past illumination conditions (De Sanctis et al. 2010; Marboeuf & Schmitt 2014). In addition, composition inhomogeneities and sublimation from icy grains may affect our understanding of coma composition.

The study of the development of cometary activity, with the goal to relate coma and nucleus chemical properties, is one of the main objectives of the Rosetta mission (Schulz 2012). Rosetta is a European Space Agency mission which encountered comet 67P/Churyumov-Gerasimenko (here-

after, referred as to 67P/C-G) in August 2014 at r_h = 3.5 AU from the Sun, and entered in a 30-km bound orbit around the comet on 9 September 2014. It will accompany 67P/C-G in its journey towards perihelion (13 August 2015, q = 1.24 AU), with the nominal mission over at the end of 2015.

The Rosetta spacecraft (S/C) is carrying a suite of eleven instruments, among which is the Visible InfraRed Thermal Imaging Spectrometer (Coradini et al. 2007). VIRTIS is composed of two channels: VIRTIS-M, a spectro-imager operating both in the visible (0.25–1 μm) and infrared (1–5 μm) ranges at low spectral resolution ($\lambda/\Delta\lambda$ = 70-380), and VIRTIS-H, a single-aperture infrared spectrometer (1.9–5.0 μm) with higher spectral resolution capabilities ($\lambda/\Delta\lambda$ = 1300–3000).

The 2–5 μm range is rich in signatures of cometary molecules. The first cometary spectrum covering this range was acquired on comet 1P/Halley with the IKS intrument aboard the VEGA-1 S/C (Combes et al. 1988). More recently, 2–5 μm spectra were acquired with the Deep Impact and EPOXI missions to 9P/Tempel 1 and 103P/Hartley 2 (A'Hearn et al. 2005, 2011), and from the Infrared Space Observatory (ISO) and the AKARI space telescope (Crovisier et al. 1997; Ootsubo et al. 2012). Infrared surveys of cometary molecules in atmospheric windows are also ongoing from ground-based facilities offering spectral resolutions > 20 000 (e.g., Dello Russo et al. 2006).

The ν_3 vibrational bands of water and carbon dioxide are the strongest vibrational bands that have been observed in cometary infrared spectra. Therefore, these two molecules were anticipated to be the first to be detected by VIRTIS. In this paper we focus on VIRTIS-H observations of H_2O and CO_2 acquired from 24 November 2014 to 24 January 2015. The observations are described in Sect.2. In Sect.3, H_2O and CO_2 column density and rotational temperature measurements are presented. Section 4 presents an upper limit on CO production. Observed H_2O and CO_2 column density variations with line-of-sight orientation in the nucleus body frame and solar illumination are discussed in Sect. 5. Measurements are then compared to gas dynamics calculations of the inner coma of 67P/C-G (Sect. 6). A conclusion follows in Sect. 7.

2. Observations

2.1. VIRTIS-H

VIRTIS-H is a cross-dispersor spectrometer, working in the range 2–5 μm. Its design consists of a telescope, an entrance slit, followed by a collimator, and a prism separating eight orders of a grating (Drossart et al. 2000; Coradini et al. 2007). The spectral resolving power $\lambda/\Delta\lambda$ varies between 1300 and 3000 within each order, where $\Delta\lambda$ is the convolution of the channel spacing and grating resolution. The spectra are sampled on 3456 spectral elements, i.e., 432 in each grating order. The spectral range covered by each order is given in Table 1.

As most Rosetta instruments, the line of sight of VIRTIS is along the Z-axis of the S/C. The instantaneous field of view of the VIRTIS-H instrument is 0.58×1.74 mrad^2 (the larger dimension being along the Y axis) which corresponds to 17×52 m on the comet for a S/C distance of 30 km.

Table 1. VIRTIS-H grating orders.

order	λ_{min}	λ_{max}
	(μm)	
0	4.049	5.032
1	3.477	4.325
2	3.044	3.774
3	2.703	3.368
4	2.432	3.077
5	2.211	2.755
6	2.024	2.526
7	1.871	2.331

The field of view (FOV) corresponds to a 3-pixel wide area on the focal plane array; in nominal mode, the summation of the signals received on each pixel is performed on-board.

The VIRTIS-H data are processed using the so-called CALIBROS pipeline. This pipeline subtracts dark images, corrects the instrumental and detector effects (odd/even pixels effects, despiking), calibrates the absolute flux of the spectra in radiance (W/m^2/sr/μm) and saves the data in the format of the Planetary Data System.

The transfer function is derived from a dual approach using both on-ground and flight data. In a first step, the transfer function was derived from laboratory calibration measurements. Because spectral registration was found to be significantly modified after launch, consistency adjustments were made using observations of asteroid (21) Lutetia obtained during the Rosetta CRUISE phase in July 2010 (Coradini et al. 2011), yielding the current transfer function. This includes precise determination of the map of illuminated pixels, correction for stray light, and accurate dark current interpolation in the flight configuration.

Hereafter, VIRTIS-H calibrated data are referred as to "cubes" because they are 3-dimensional : intensity versus wavelength and acquisition number.

2.2. Dataset

Rosetta observations of 67P/C-G are grouped in Medium Term Planning periods (MTP), typically lasting one month, and Short Term Planning periods (STP), lasting one week. The first dedicated coma observations of 67P/C-G with VIRTIS were obtained during MTP005 (28 July 2014, at 3.7 AU from the Sun). Observations carried out from August to September do not show any detection of molecular bands. Only marginal detections of H_2O and CO_2 were obtained in October 2014 (MTP008) before Philae-landing operations (MTP009). Therefore, we focus on coma observations undertaken between 24 November 2014 and 24 January 2015 (MTP010 to MTP012). Table 2 lists the VIRTIS-H data cubes analysed in this paper, the observation dates and geometric parameters. During this time frame, Rosetta was on a terminator orbit around the comet (phase angle in the range 80–100°) at distances between 18 and 30 km from the comet centre. The heliocentric distance range was r_h = 2.47–2.91 AU. The VIRTIS-M spectro-imaging channel was operated in parallel to

VIRTIS-H for coma mapping (Capaccioni et al. 2015a). The analysis of the VIRTIS-M data will be the topic of a forthcoming paper.

VIRTIS-H observations were acquired with an acquisition time of 6 s, both on the source and on the dark background. A dark rate of 4 (i.e., one dark image every 4 acquisitions on-source) was determined to be optimum for signal-to-noise considerations. Some data were acquired with dark rates of 2, 8 and 16 to find this optimum. Because of data volume restrictions, on-board frame summing was occasionally performed.

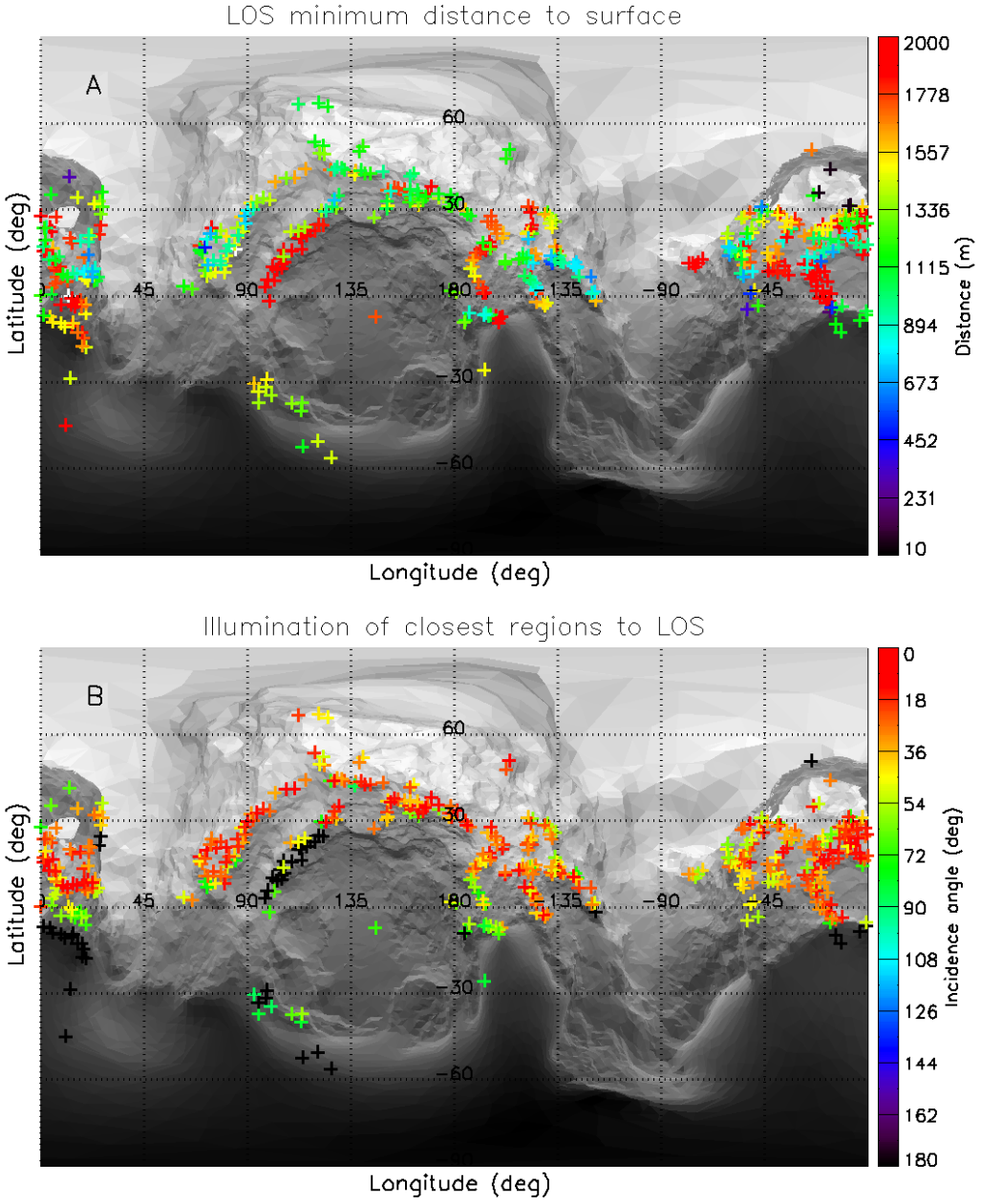

Fig. 1. Geometrical parameters of the VIRTIS-H line of sight from MTP010 to MTP012. A) Minimum distance of the LOS to the nucleus surface (in meters with the color scale given to the right); B) Corresponding solar incidence angle (in degrees, with the color scale given to the right). Each cross corresponds to a single acquisition. The grey-color background represents the effective latitude based on SHAP5 model composed of 300 000 facets to show the location of topographic features.

2.3. Pointing geometry and limb distance

Requested limb distances (defined as the closest distance from the line of sight (LOS) to the nucleus) were typically 0.5–1 km. Pointing requests for these coma observations were designed so that the FOV would not intercept the nucleus, and therefore took into account expected uncertainties in the S/C pointing provided by the ESA Rosetta Science Ground Segment.

We only consider here observations with the FOV staring at a fixed position in inertial frame (in general limb offset in the solar direction) during cube acquisition. A few cubes during MTP011 were acquired with more complex pointing strategies and are not analysed here. We do not consider either cubes with the LOS in the nucleus shade, since low molecular signals are expected because of ineffective radiative IR pumping. Cube 00377746075 (STP035) is however partly affected by shading (at the 20% level in number of acquisitions).

Because of S/C pointing errors, the LOS was sometimes intercepting the nucleus during the observations. Table 2 provides for each cube, the total number of acquisitions $n_{\rm acq}$, and the number of acquisitions $n_{\rm coma}$ not intercepting the nucleus. Throughout this paper we are considering only acquisitions not intercepting the nucleus. The overall observing time (Δt) and the cumulated exposure time on the coma (Int.) are also provided in Table 2, for each data cube. Δt is 2 to 3 hours in average, that is less than one fourth the nucleus rotation period of 12.40 h (Sierks et al. 2015).

The actual limb distance and orientation of the LOS in the comet inertial frame were determined using a digital shape model of the surface combined with S/C attitude data, and S/C and 67P/C-G trajectories. This was done using the SPICE library (Acton 1996)[1]. The shape model was produced by the Optical, Spectroscopic, and Infrared Remote Imaging System (OSIRIS) imaging team for use within the Rosetta project (Sierks et al. 2015). The SHAP5 version (cg-spc-shap5-v0.1-esoc.bds) was used for our purpose. The shape model was also used to compute the solar illumination of the nucleus regions close to the LOS. This LOS characterization was done using smoothed versions of SHAP5 ($\sim$ 6290 and 31456 triangular facets instead of several millions), since a detailed description of the nucleus local topography would provide unnecessary precision.

During data acquisition, the LOS moved with respect to the body-fixed frame, mainly because of nucleus rotation. Figure 1 shows the locations of the closest points to the LOS in the (long, lat) 67P/C-G coordinates, and the local solar incidence angle at these points at the time of the observations. The minimum distance of the LOS to the surface varied from 10 m to $\sim$ 1500 m (Fig. 2A). The distribution of the LOS minimum distances presents two maxima, resulting from the complex shape of the 67P/C-G nucleus (Fig. 2A). The solar incidence angle ranged from 0° to 180°, with most values within 0–50° since observations focused on the summer (northern) hemisphere in day time (Fig. 1, Fig. 2B).

67P's nucleus has two lobes, referred to as the "head" and "body", respectively, linked by the "neck", in reference to the duck-like shape of the nucleus (Sierks et al. 2015). The central longitudes

[1] http://naif.jpl.nasa.gov/naif/

Table 2. Log of the observations.

Obs Id	Start time (UT)	Stop time (UT)	Δt (hr)	Int. (hr)	Δ(S/C) (km)	r_h (AU)	Phase °	n_{coma} / n_{acq}	D(LOS) (km)
MTP010	*STP030*								
00375410695	2014-11-24 00:31:59.0	2014-11-24 04:51:45.7	4.33	1.92	29.1	2.913	81.3	916/1152	2.39
00375453895	2014-11-24 12:31:59.0	2014-11-24 16:51:45.7	4.33	1.92	28.9	2.909	80.8	913/1152	2.43
MTP010	*STP031*								
00375818995	2014-11-28 17:56:59.3	2014-11-28 22:45:40.0	4.81	2.13	28.8	2.880	81.9	825/1280	2.75
MTP010	*STP032*								
00376211338	2014-12-03 07:01:53.0	2014-12-03 08:52:10.2	1.84	1.39	27.3	2.849	88.7	832/ 832	2.64
00376302843	2014-12-04 08:26:57.8	2014-12-04 10:17:15.0	1.84	1.39	23.0	2.842	88.9	670/ 832	2.69
00376466638	2014-12-06 05:56:53.1	2014-12-06 06:47:40.3	0.85	0.64	18.8	2.829	82.4	384/ 384	2.45
00376470838	2014-12-06 07:06:53.0	2014-12-06 07:57:40.2	0.85	0.64	18.8	2.828	82.6	384/ 384	2.63
00376670763	2014-12-08 14:38:58.0	2014-12-08 16:29:15.2	1.84	1.39	18.2	2.812	81.4	832/ 832	2.75
00376683791	2014-12-08 17:57:17.3	2014-12-08 21:10:07.9	3.21	0.75	18.4	2.811	81.4	448/ 448	2.58
00376706343	2014-12-09 00:31:58.0	2014-12-09 02:22:15.2	1.84	1.39	18.6	2.809	81.3	832/ 832	2.50
00376769292	2014-12-09 18:01:58.0	2014-12-09 19:56:30.2	1.91	1.60	19.0	2.804	88.3	735/ 960	2.22
MTP010	*STP033*								
00377183691	2014-12-14 13:02:02.5	2014-12-14 15:26:07.0	2.40	1.07	17.9	2.771	87.6	523/ 640	2.50
00377201041	2014-12-14 17:56:56.1	2014-12-14 19:13:13.4	1.27	0.96	18.1	2.769	87.4	576/ 576	2.23
00377209498	2014-12-14 20:12:02.6	2014-12-14 22:36:13.4	2.40	1.07	17.8	2.768	82.8	512/ 640	2.79
MTP010	*STP034*								
00377442541	2014-12-17 13:01:56.2	2014-12-17 14:26:43.5	1.41	1.07	19.1	2.750	85.8	640/ 640	2.23
00377451721	2014-12-17 15:34:56.2	2014-12-17 17:16:43.4	1.70	1.28	19.2	2.749	80.8	768/ 768	2.46
00377460591	2014-12-17 17:57:02.6	2014-12-17 20:21:07.0	2.40	1.07	19.1	2.748	80.4	640/ 640	2.43
MTP011	*STP035*								
00377678521	2014-12-20 06:34:56.3	2014-12-20 09:24:43.5	2.83	2.13	18.6	2.730	85.1	1280/1280	2.62
00377693120	2014-12-20 10:38:15.4	2014-12-20 12:54:02.7	2.26	1.71	18.6	2.729	85.3	1024/1024	2.39
00377746075	2014-12-21 01:15:00.1	2014-12-21 05:20:19.9	4.09	1.81	19.8	2.724	90.6	1047/1088	2.98
00377766356	2014-12-21 06:53:00.8	2014-12-21 10:14:59.7	3.37	1.49	20.2	2.723	87.8	896/ 896	2.96
MTP011	*STP036*								
00378023941	2014-12-24 06:31:56.4	2014-12-24 09:04:43.6	2.55	1.92	24.8	2.702	83.8	1152/1152	2.84
00378037917	2014-12-24 10:24:52.3	2014-12-24 12:49:09.6	2.40	1.81	24.5	2.701	84.6	1088/1088	2.69
00378047341	2014-12-24 13:01:56.4	2014-12-24 13:52:43.7	0.85	0.64	24.9	2.700	84.3	384/ 384	2.61
00378053606	2014-12-24 14:46:21.7	2014-12-24 18:52:38.9	4.10	3.09	24.5	2.699	85.0	1856/1856	2.60
00378326101	2014-12-27 18:27:56.5	2014-12-27 21:09:13.8	2.69	2.03	26.4	2.677	85.6	1216/1216	2.62
00378340674	2014-12-27 22:24:59.0	2014-12-28 00:49:09.8	2.40	1.07	26.4	2.675	85.4	640/ 640	2.60
00378446992	2014-12-29 04:03:38.6	2014-12-29 06:51:43.8	2.80	2.35	26.6	2.667	86.3	365/1408	4.29
MTP011	*STP037*								
00378954841	2015-01-04 01:06:56.8	2015-01-04 01:57:44.0	0.85	0.64	26.9	2.624	79.8	384/ 384	2.63
00378963263	2015-01-04 03:21:28.1	2015-01-04 06:57:53.9	3.61	1.60	26.9	2.623	81.5	960/ 960	2.66
00378981052	2015-01-04 08:17:57.1	2015-01-04 11:54:23.0	3.61	1.60	26.8	2.622	79.8	960/ 960	2.50
00378996383	2015-01-04 12:39:18.7	2015-01-04 12:56:05.9	0.28	0.21	26.8	2.621	81.9	128/ 128	2.20
MTP012	*STP039*								
00379861738	2015-01-14 13:01:54.3	2015-01-14 14:43:41.6	1.70	1.28	26.3	2.548	80.5	768/ 768	3.03
00379870181	2015-01-14 15:22:37.3	2015-01-14 17:04:24.6	1.70	1.28	26.5	2.547	80.5	768/ 768	3.21
00379877117	2015-01-14 17:18:12.8	2015-01-14 19:51:00.1	2.55	1.92	26.6	2.546	79.5	1152/1152	3.29
00379896840	2015-01-14 22:46:56.0	2015-01-15 00:11:43.2	1.41	1.07	26.7	2.545	79.3	640/ 640	3.45
00380098435	2015-01-17 06:46:51.4	2015-01-17 09:19:38.5	2.55	1.92	27.0	2.528	79.2	1152/1152	3.48
00380112315	2015-01-17 10:38:11.3	2015-01-17 11:28:58.5	0.85	0.64	27.1	2.527	81.2	384/ 384	2.75
00380115835	2015-01-17 11:36:51.3	2015-01-17 12:53:08.5	1.27	0.96	27.0	2.526	79.4	576/ 576	3.43
00380228935	2015-01-18 19:01:51.4	2015-01-18 20:43:38.6	1.70	1.28	26.6	2.517	79.7	768/ 768	3.34
00380257831	2015-01-19 03:03:27.4	2015-01-19 06:52:44.6	3.82	2.88	26.6	2.514	80.0	1728/1728	3.29
MTP012	*STP040*								
00380459084	2015-01-21 10:50:58.5	2015-01-21 13:54:15.4	3.05	1.28	26.2	2.497	80.6	767/ 768	3.37
00380701735	2015-01-24 06:21:51.5	2015-01-24 09:20:08.7	2.97	2.24	26.3	2.476	80.6	1344/1344	3.41
00380717118	2015-01-24 10:38:14.2	2015-01-24 12:11:31.5	1.55	1.17	26.2	2.475	81.8	704/ 704	3.04
00380723637	2015-01-24 12:26:53.8	2015-01-24 14:25:41.0	1.98	1.49	26.2	2.474	80.8	896/ 896	3.26
00380733205	2015-01-24 15:06:21.6	2015-01-24 17:47:38.8	2.69	2.03	26.2	2.473	81.9	1216/1216	2.81
00380743438	2015-01-24 17:56:54.4	2015-01-24 19:30:11.6	1.55	1.17	26.1	2.473	81.0	704/ 704	3.20
00380758438	2015-01-24 22:06:54.3	2015-01-25 00:31:11.6	2.40	1.81	26.0	2.471	81.6	1088/1088	3.27

Note: Δt is the elapsed time between the start and stop times; Int. in the integration time on source; Δ(S/C) is the spacecraft distance to comet centre; r_h is the heliocentric distance; Phase is the phase angle; n_{coma} and n_{acq} are the number of acquisitions in the coma, and total number of acquisitions, respectively, D is the distance of the LOS to comet centre, as defined in Sect. 5.1.

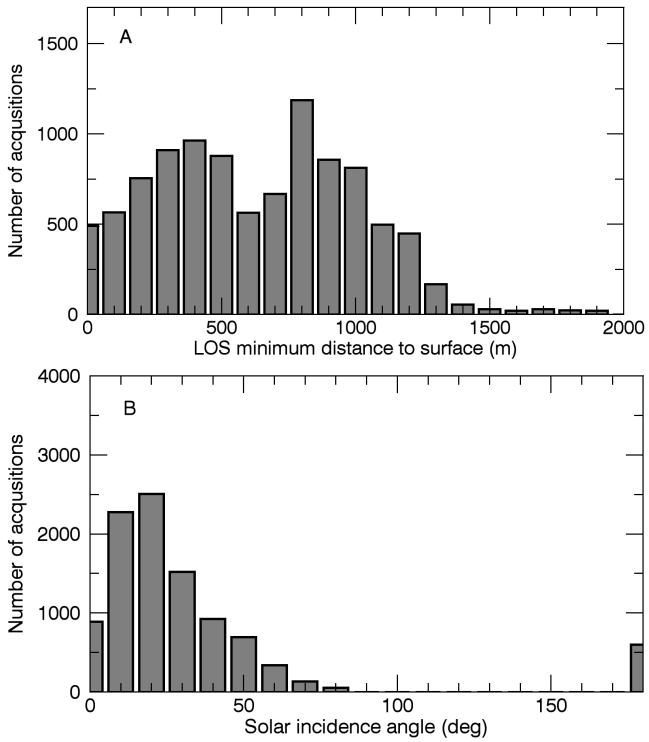

Fig. 2. LOS statistics from MTP010 to MTP012. A) Minimum distance of the LOS to the nucleus (in meter, bin size is 100 m); B) Corresponding solar incidence angle (bin size is 10°).

of the head and body are approximately 340° and 135°, respectively, in the SHAP5 coordinate system (Fig.1). The orientations of the LOS in the body-fixed frame are further discussed in Sect. 5.

3. H_2O and CO_2 spectra, column densities, and rotational temperatures

The ν_3 bands of H_2O and CO_2, at 2.67 and 4.27 μm, respectively, were the first vibrational bands expected to be detected by VIRTIS. Indeed, H_2O is the main molecule in cometary atmospheres, and was first detected in 67P/C-G at 3.92 AU from the Sun (6 June 2014) by the Microwave Instrument of the Rosetta Orbiter (MIRO) with a total production rate estimated to be 1×10^{25} s^{-1} (Gulkis et al. 2014, 2015). CO_2 was detected by the Rosetta Orbiter Spectrometer for Ion and Neutral Analysis (ROSINA) instrument onboard Rosetta (Hässig et al. 2015). Though CO_2 is less abundant than H_2O, the CO_2 band is relatively easier to detect than the H_2O band because its band strength is ten times higher. We considered only spectra acquired in orders 0 and 4 of VIRTIS-H (Table 1) for the analysis of the CO_2 and H_2O bands, respectively, as these bands are only partially covered in adjacent orders (order 1 for CO_2 and orders 3 and 5 for H_2O).

The ν_3 bands of both H_2O and CO_2 were first detected by VIRTIS-H at the beginning of October, by averaging several data cubes[2](Fig. 3). In the December-January time frame, both bands were detected with signal-to-noise ratios (SNR) on the band area reaching 40 on individual data cubes (Table 3). Figure 4 shows an average spectrum of H_2O, combining 35 data cubes acquired from 4 December 2014 to 24 January 2015. For this figure, we selected the data cubes with a SNR

[2] Averaged data cubes are: 00371530649, 00371674954, 00372295949, 00371228249, 00371647949, 00371763968, 00372526349, 00371285849, 00371662348, and 00372180750.

on the CO_2 band area larger than 10. The SNR in the H_2O average spectrum shown in Fig. 4 is 135. The CO_2 spectrum obtained averaging the same 35 cubes is shown in Fig. 5, and has a SNR of 123.

At the spectral resolution of VIRTIS-H, the ro-vibrational structure of the H_2O ν_3 band is partly resolved (Figs 3–4), which provides us information on the rotational temperature of water (Sect. 3.2). Note that the ten times weaker ν_1 band lies partly in the spectral range of ν_3 (Bockelée-Morvan & Crovisier 1989; Villanueva et al. 2012) and is considered in the synthetic H_2O spectra shown in Figs 3 and 4.

The P, R structure of the CO_2 ν_3 band is resolved, but not the individual P and R ro-vibrational lines (Fig. 5).

The H_2O and CO_2 band intensities are given in Table 3. For H_2O, they were derived by summing the radiances measured in wavelength intervals within 2.60–2.73 μm where significant water emission was expected. For CO_2, the summation is made over 4.23–4.285 μm. A 4th order polynomial baseline was subtracted from the spectra before the summation.

3.1. H_2O and CO_2 column densities

The determination of the H_2O and CO_2 column densities from the measured band intensities (Table 3) is straightforward because optical depth effects are expected to be non significant (Debout et al. 2015), given the low activity of comet 67P/C-G at the time of the observations (production rate around 10^{26} s^{-1}, Sect. 6). The main excitation mechanism for these bands is expected to be fluorescence excited by solar infrared radiation (Crovisier 1987; Bockelée-Morvan 1987; Bockelée-Morvan et al. 2004). The column density $< N >$ (m^{-2}) is related to the band intensity I (in W m^{-2} sr^{-1}) through:

$$I = \frac{h\nu}{4\pi} g_{\rm f} < N > \quad (1)$$

where ν is the central frequency of the band, and $g_{\rm f}$ is the band emission rate (or g-factor).

We assumed a g-factor $g_{\rm f} = 3.349 \times 10^{-4}$ s^{-1} and $g_{\rm f} = 3.33 \times 10^{-5}$ s^{-1} (at r_h = 1 AU) for the H_2O ν_3 and ν_1 bands, respectively (Villanueva et al. 2012). Ro-vibrational lines of the ν_2+ν_3–ν_2 H_2O band are present in the 2.6–2.73 μm range where the band intensity was calculated, but they do not contribute significantly to the observed emission (Bockelée-Morvan & Crovisier 1989; Villanueva et al. 2012). The 2.6–2.73 μm range covers 77% of the sum of the ν_1 and ν_3 band intensities at a rotational temperature $T_{\rm rot}$ = 90 K which approximates the excitation state of water observed by VIRTIS-H (Sect. 3.2). This factor was taking into account for the determination of the water column densities.

As for CO_2, we used a g-factor at r_h = 1 AU of 2.69×10^{-3} s^{-1} (Debout et al. 2015). The 4.23–4.285 μm range used for band intensity measurements covers 88.4% of the total ν_3 band emission for $T_{\rm rot}$ = 90 K, and this factor was applied.

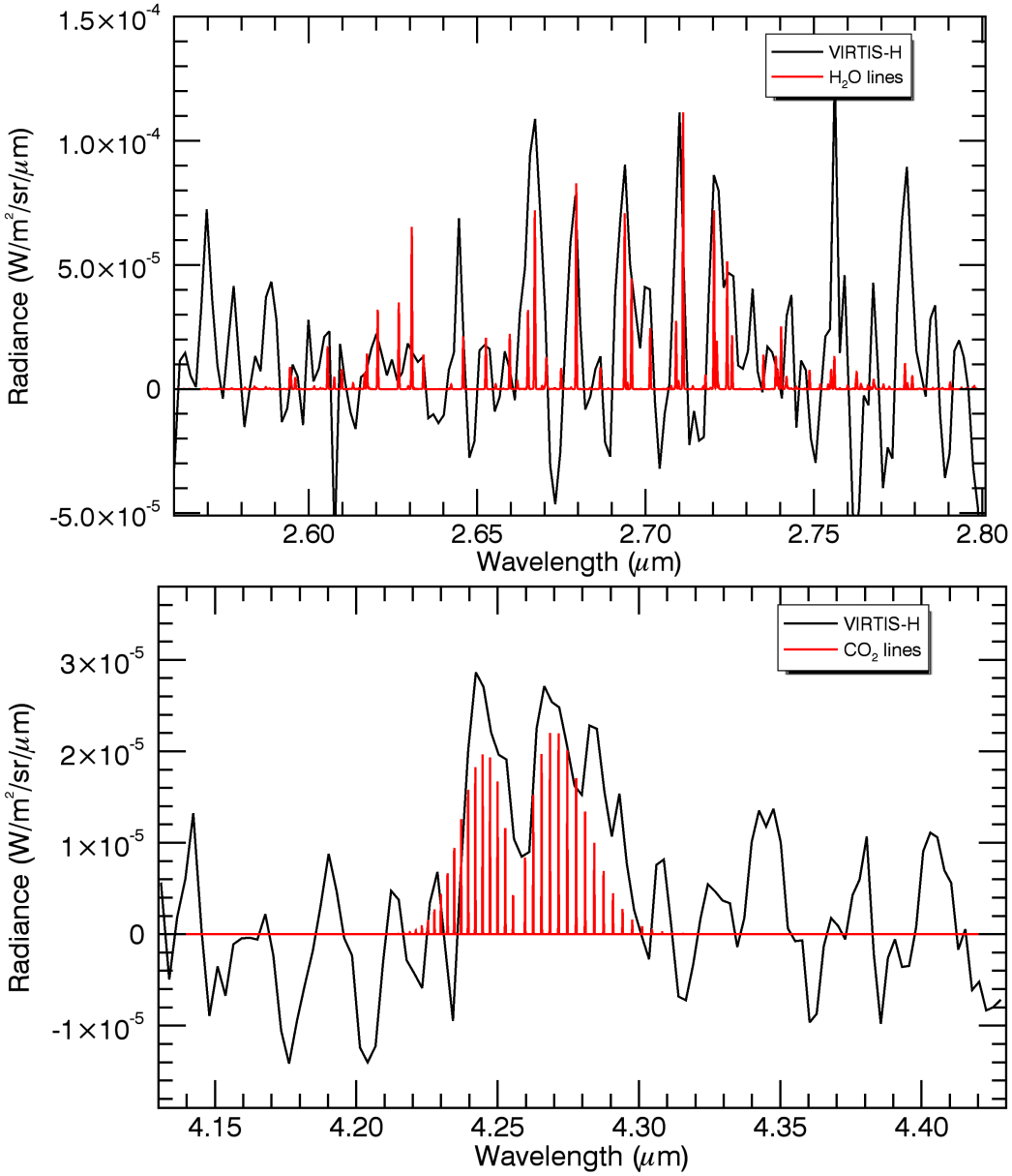

Fig. 3. VIRTIS-H average spectra of H_2O and CO_2 bands observed from 10 to 17 October 2014, in spectral orders 4 and 0, respectively. Superimposed a model spectrum of the ro-vibrational structure of H_2O (ν_1 and ν_3) and CO_2 ν_3 bands.

The derived column densities are given in Table 3, and plotted as a function of time in Fig. 6 (left). A power-law fit to the values (not considering upper limits) leads to a heliocentric variation in $r_h^{-0.9}$ for water and in $r_h^{+1.3}$ for CO_2, suggesting a small increase of 67P/C-G water outgassing between 2.88 and 2.47 AU (15% in average), whereas the CO_2 production slightly decreases. Admittedly, this study is biased by several effects (e.g., various limb distances, LOS geometry, solar illumination conditions of the nucleus, uneven distribution of data throughout the period), but it is worth recalling that Rosetta remained on a terminator orbit in this time frame. Power-law fits to smaller data sets (selecting LOS above regions of similar illumination conditions) lead to similar conclusion, i.e., that the activity of 67P/C-G did not change much from 2.9 to 2.5 AU.

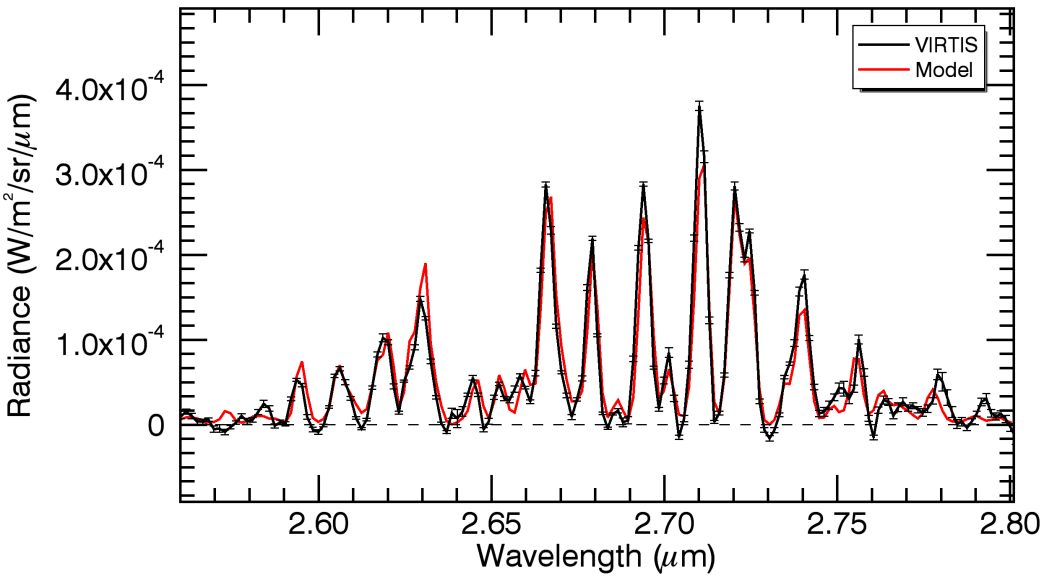

Fig. 4. VIRTIS-H spectrum of the 2.67 μm band of water. Average of 35 data cubes with most significant water and CO_2 detections (those with SNR > 10). Superimposed a model spectrum of H_2O band (ν_1 and ν_3) for a rotational temperature T_{rot} = 102 K (see text). The effective spectral resolution, derived from fitting, is R_{eff} = 800.

3.2. Band fitting and rotational temperature

Model fitting of the H_2O and CO_2 bands was performed through χ^2 minimization of fluorescence excitation models (Debout et al. 2015), with the rotational temperature T_{rot}, the column density $< N >$, and the effective spectral resolution R_{eff} as free parameters.

For H_2O, both the ν_1 and ν_3 bands were considered. Excitation of these bands is mainly through direct infrared solar pumping from the ground vibrational state. However, for the ν_1 band, spontaneous cascades from higher-energy excited vibrational states (mainly the combination band $\nu_1+\nu_3$)

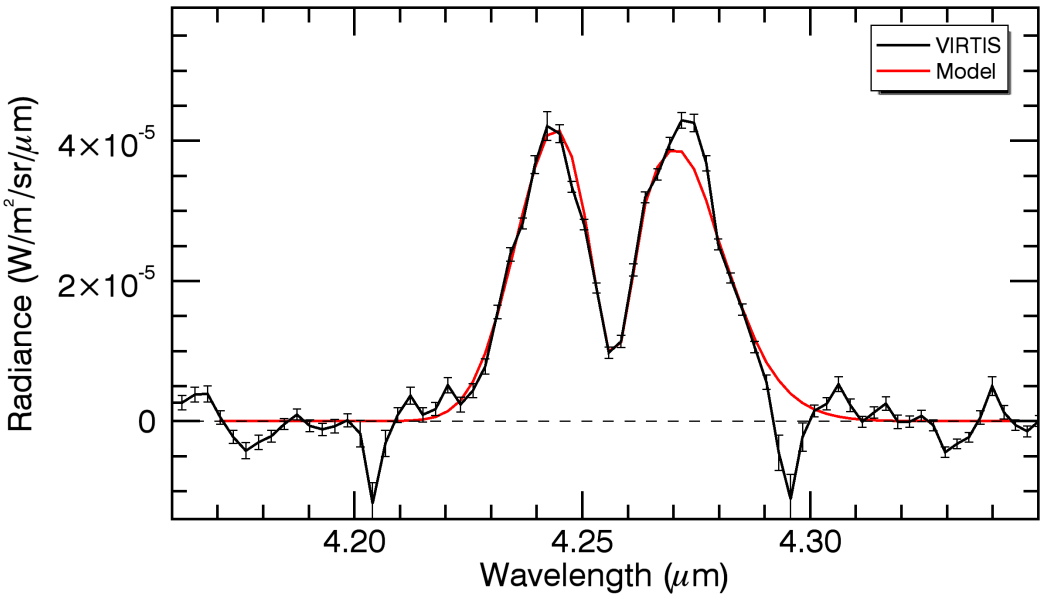

Fig. 5. VIRTIS-H spectrum of CO_2 band at 4.27 μm. Average of 35 data cubes with most significant water and CO_2 detections (SNR > 10). Superimposed a model spectrum of the ν_3 CO_2 band for T_{rot} = 90 K. The effective spectral resolution, derived from fitting, is R_{eff} = 869.

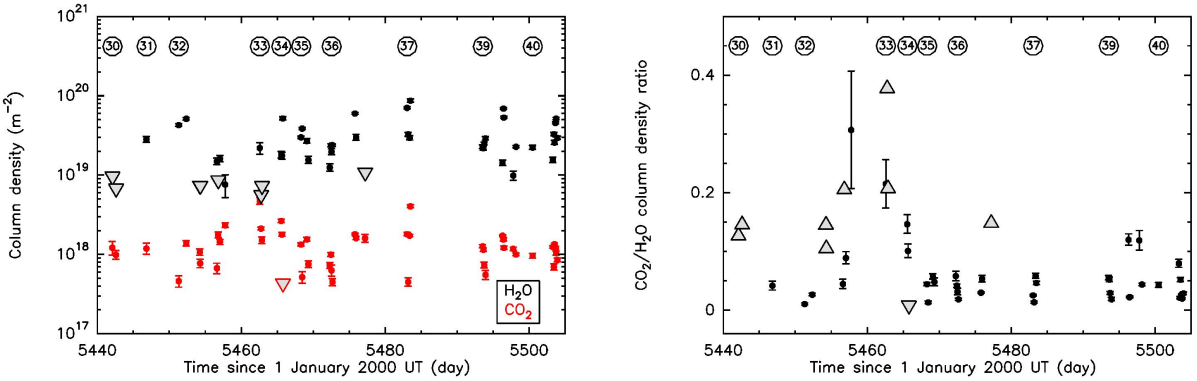

Fig. 6. H_2O and CO_2 column densities (left), and column density ratio $< N(CO_2) > / < N(H_2O) >$ (right) as a function of time. Symbols for upper and lower limits are downward and upperward triangles, respectively. The STP periods are indicated in the top, inside circles.

are significant, increasing by a factor of 2.0 the ν_1 g-factor (for emission) with respect to the resonant-fluorescence value (Bockelée-Morvan & Crovisier 1989; Villanueva et al. 2012). The fluorescence model used for fitting the VIRTIS-H water band does not consider combination bands and subsequent spontaneous decays, but assumes a relative ν_1/ν_3 emission rate of 0.10 given by full non-resonance fluorescence models (Villanueva et al. 2012). Since the contribution of the ν_1 band to the fitted spectrum is weak (~3% times the intensity of ν_3), this oversimplification should not affect the results. Resonant fluorescence is assumed for CO_2 (Debout et al. 2015). H_2O and CO_2 ν_3 ro-vibrational line strengths and frequencies were taken from the HITRAN data base (Rothman et al. 2009).

We assumed an ortho-to-para ratio (OPR) for water of 3. Indeed, the data set acquired until the end of January 2015 does not provide a precise measurement of the OPR. OPRs measured so far in comets span between 2 and 3 (Bonev et al. 2007).

Synthetic VIRTIS-H spectra were obtained by convolving modeled ro-vibrational radiances at infinite resolution with a gaussian profile of width $\Delta\lambda_{\rm eff}$, as a free parameter. The contribution of this convolved spectrum to each spectral channel was then computed taking into account their spectral response (FWHM of ~ 80% the channel spacing, e.g., FWHM ≃ 1.1 nm at 2.67 μm, Drossart et al. 2000). The derived effective spectral resolution $R_{\rm eff} = \lambda/\Delta\lambda_{\rm eff}$ is ~ 900, that is, smaller than the nominal spectral resolution, due to undersampling and some spectral broadening introduced by the current calibration scheme to correct for odd/even effects.

From the water and CO_2 spectra shown in Figs 4–5 we derive $T_{\rm rot}$ = 102 ± 4 K and 90 ± 3 K, respectively, pertaining to a mean distance to the surface of 800 m (additional errors on $T_{\rm rot}$ can be caused by non-optimized baseline retrieval). Misfits for some water ro-vibrational lines show that the population distribution in the ground vibrational state cannot be described by a Boltzmann distribution, the reason being that the considered spectrum is an average of many spectra, and that even a single LOS is sampling molecules in various excitation states (because of variations of

the kinetic temperature with position in the coma and expected non-LTE conditions in the more rarefied regions, e.g., Davidsson & Gutiérrez 2006). A feature longward 2.79 μm is not reproduced by the model, and might be from the water $\nu1+\nu3-\nu1$ hot band. There is also some unexplained discrepancy between the observed and modeled CO_2 band shape (Fig. 5).

Moderate signal-to-noise ratios make it difficult to perform $T_{\rm rot}$ retrievals from individual data cubes. However, from the cube 00380112315 (STP039) for which the SNR on the total H_2O band area is 40 (Table 3), we derive $T_{\rm rot}$ = 96 ± 4 K. During the acquisition of these data, the LOS remained above the neck region (Sect. 7), with a mean distance to the centre of 67P/C-G of D = 2.73 km (as defined in Sect. 5.1), i.e. at 730 m in average from the surface.

The measured rotational temperatures are indicative of the temperature of the gas sampled by the line-of-sight. Indeed, we performed calculations of the population distribution of the H_2O ground vibrational state taking into account both collisions and radiative decay (Zakharov et al. 2007), which show that the lowest ground-state rotational levels (up to J =5) remain thermalized at the temperature of the gas for distances that exceed a few kilometers from the nucleus surface. For these calculations, we assumed isotropic water production rate at a rate of 10^{26} s^{-1} (Sect. 6). Moreover, the similarity of the rotational temperatures of H_2O and CO_2 is consistent with near-LTE conditions for both species. Indeed, in a more rarefied coma, a higher $T_{\rm rot}$ would have been measured for CO_2 since rotational radiative decay is ineffective for this species.

The measured rotational temperatures are close to expected values for 67P/C-G at 2.5 AU from the Sun (Davidsson et al. 2010). In the Monte Carlo simulations presented in Sect. 6, which provide an overall good reproduction of measured column densities, the gas temperatures on the day side are typically about 100 K at 500 m above the surface and about 75 K at 1500 m above the surface, with higher values above the neck regions. This is overall consistent with VIRTIS measurements, keeping in mind that the FOV of VIRTIS is probing molecules at various distances from the nucleus.

4. CO ν(1–0) band observations

Carbon monoxide has been identified as a significant compound of the coma of 67P/C-G, with a CO/CO_2 relative amount in number at Rosetta S/C in the range ~ 0.5–5 in August–September 2014 (Hässig et al. 2015). However, CO is more difficult to detect than CO_2 with VIRTIS as its band strength is one order of magnitude lower than the CO_2 band.

The ν(1–0) band of CO at 4.67 μm lies in the spectral range of grating order 0, as the CO_2 band (Table 1). Using the HITRAN data base (Rothman et al. 2009), and using the solar flux given by Labs & Neckel (1968), we derived a band g-factor g_f = 2.485 × 10^{-4} s^{-1}, at 1 AU from the Sun, for a rotational temperature of 90 K (Debout et al. 2015). The VIRTIS-H spectrum obtained by averaging the 35 cubes where CO_2 is detected with a SNR > 10 does not show significant CO emission. From this spectrum, we derive upper limits of 80% (3σ) for the $< N_{\rm CO} > / < N_{\rm CO_2} >$ ratio, and of 1.9% (3σ) for the $< N_{\rm CO} > / < N_{\rm H_2O} >$ ratio, whereas the $< N_{\rm CO_2} > / < N_{\rm H_2O} >$ ratio is 2.5%.

Large variations of the CO/CO_2 number density ratio were observed by ROSINA in August-September 2014, with the highest values (up to ~ 5) observed in August, when the S/C Z axis was towards the northern (summer) hemisphere (Hässig et al. 2015), i.e., at the latitudes sampled by VIRTIS. However, comparing VIRTIS values to these ROSINA results is difficult since observation times are different and ROSINA in situ measurements were done at distances from the comet > 80 km.

5. H_2O and CO_2 production versus morphological regions and illumination

The large scatter in column densities and CO_2/H_2O column density ratio seen in Fig. 6 is related to the various LOS configurations in the nucleus-fixed frame, together with different illumination conditions of 67P/C-G nucleus. We characterized the mean LOS for each cube, using the morphological regions defined by Thomas et al. (2015). 67P/C-G nucleus displays a large heterogeneity, and the northern hemisphere can be divided into nineteen geographical regions with specific morphological characteristics (Thomas et al. 2015). Regions are listed in Table 4 and labelled from 1 to 22. Regions on the bottom of the 'body' are Imhotep (13), Khepry (14), Aten (6), and part of Ash (5), with Ash, Aker (1), Anubis (2), Apis (4), Atum (8), Babi (9), and Seth (19), located in more central parts. Regions on the top of the 'head' are Hatmehit (12), Maftet (16), Nut (17), and parts of Bastet (10) and Ma'at (15), with Ma'at, Hathor, Anuket (3), and Serqet (18) in central parts. The region in the neck is named Hapi (11). Un-named dark regions near the terminator are labelled 20 to 22. The location of the regions in 2D and 3D nucleus representations are shown in Fig. 7.

For each acquisition in the cubes, we computed the solid angle of each region, as seen from the closest point of the LOS to the comet centre. This was done by determining the facets in the shape model belonging to each region and their solid angle. We then averaged the results obtained for all cube acquisitions to obtain the mean solid angle Ω_m for the cube. Regions viewed with the largest solid angle (P1) from this point, or in second positions (P2) are indicated in Table 3.

Table 4 lists for each region the number of cubes they are appearing in P1 and P2. The nucleus was obviously not evenly covered (see also Fig.1), with only 14 regions appearing in P1 or P2. Some regions, like Hapi, are often far in the classification because of their small surface area.

The mean illumination of the nucleus, as seen from this LOS location, is computed by weighting the illumination of each facet by their solid angle, with the illumination defined by the cosine of the solar incidence angle at the facets (set to 0 for solar incidence angles $i > 90°$). The arc cosine of this mean illumination defines the mean solar incidence angle at the nucleus (further referred as to solar incidence angle).

5.1. CO_2 and H_2O columns

Column densities as a function of mean nucleus illumination as seen from the LOS are shown in Fig 8. The largest values for H_2O (those larger than 4×10^{19} m^{-2}, so 2 to 4 times the average value of the remaining sample) are for LOS above Seth (red), Anuket (pale pink), and Hapi (light green),

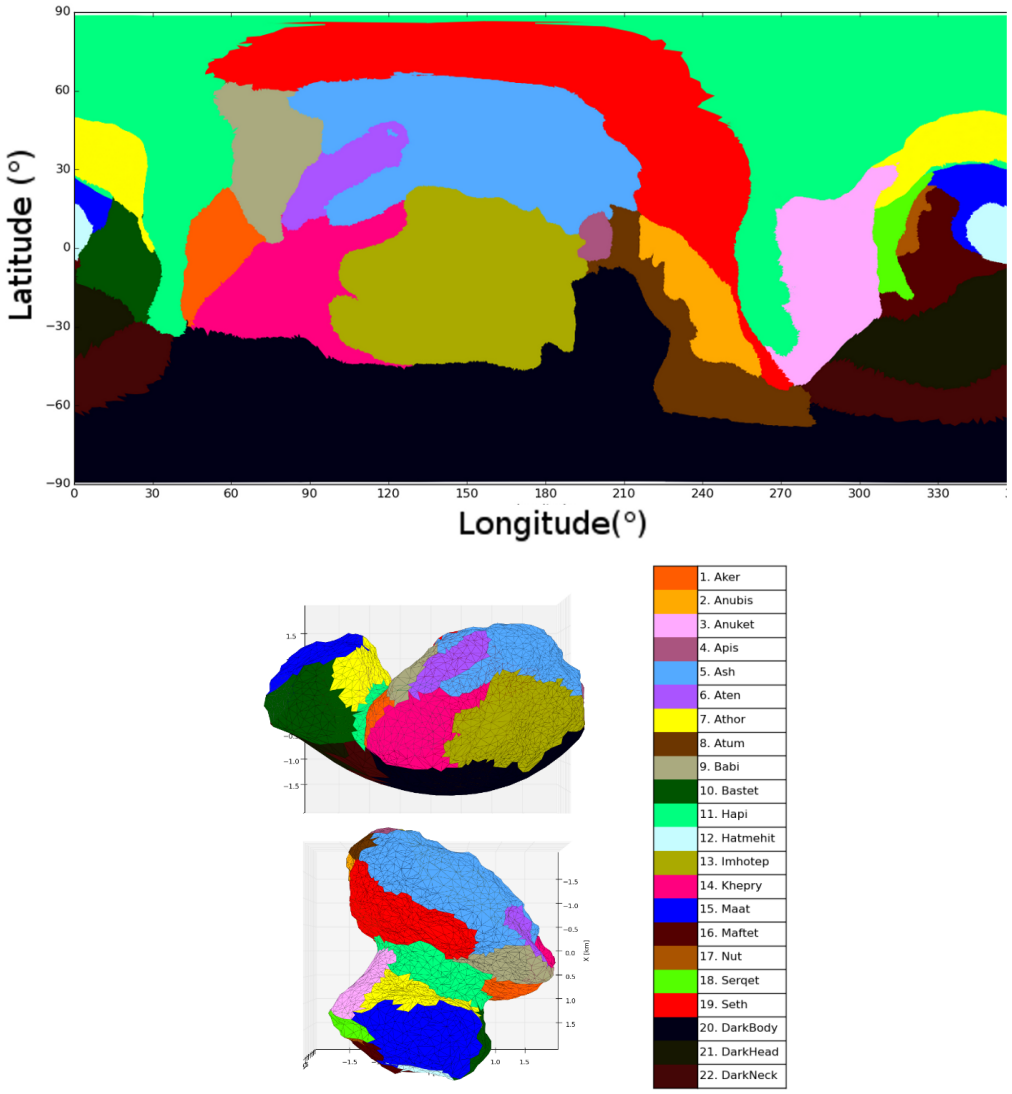

Fig. 7. Geomorphological regions of 67P/C-G in 2D and 3D visualisation (after Thomas et al. 2015).

i.e. sampling coma regions above the neck where large dust activity has been observed from the OSIRIS cameras (Sierks et al. 2015).

In Fig. 9, we applied a factor to column densities to correct for both the distance of the LOS to the nucleus, and the nucleus cross-section S viewed from the closest LOS point to nucleus centre. Here, we are making the assumption that the column density scales as S/D, where D is the distance to the centre of a sphere of radius $r_n = 2$ km (the equivalent radius of 67P/C-G nucleus), sustaining the solid angle Ω_m. This scaling is expected in the frame of the Haser model, and assumes that the gas velocity is the same everywhere. The nucleus cross-section is given by $S = \Omega_m \times D^2$. The corrected water column density still shows excess above Seth, Anuket and Hapi (Fig. 9). This suggests that these regions are the most productive in water, in line with conclusions obtained from data acquired with MIRO (Biver et al. 2015; Lee et al. 2015; Gulkis et al. 2015) and consistent with the dust distribution around the nucleus (Sierks et al. 2015). For CO_2, only one data cube exhibits a

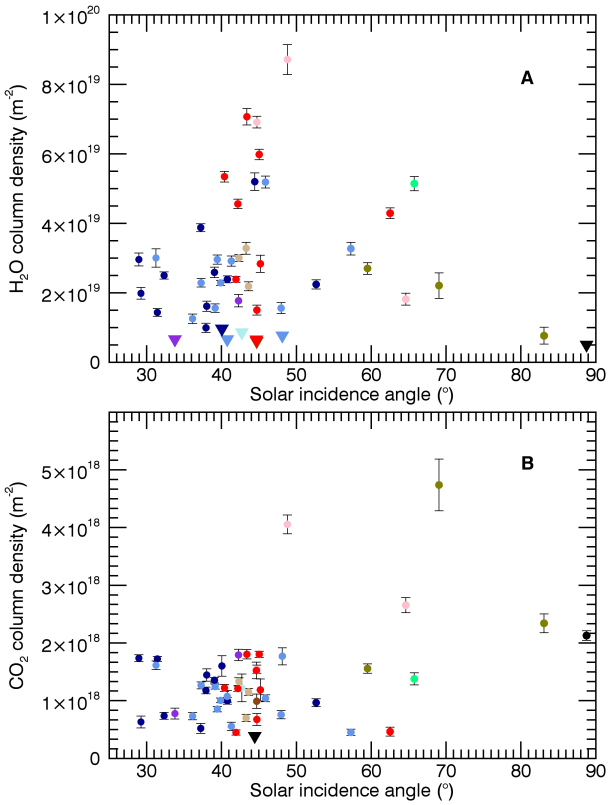

Fig. 8. Column densities as a function of mean nucleus solar insolation for regions populating the LOS. A) H_2O, B) CO_2. Color coding is that of Fig. 7 and corresponds to regions in P1.

high column density (Anuket at 50° illumination) when a high water column is measured, with the result that the lowest column density ratios are observed for these above-neck LOS (see Sect. 5.2).

The dataset is too limited to investigate in detail variations of gas production with local illumination, except for LOS above Imhotep and dark (un-named) regions, observed with solar incidence angle larger than 60°, in average. However:

- A possible trend for lower H_2O column density at lower illuminations is observed (Fig. 9A). Given the relatively high sublimation temperature of H_2O, together with the strong diurnal temperature variations of 67P/C-G surface (Capaccioni et al. 2015b; Tosi et al. 2015), we do not expect significant water outgassing in non-illuminated area.
- The corrected CO_2 column density does not show much trend with solar incidence (though a high value for Imhotep is observed, Fig. 9B), suggesting that CO_2 is outgassing from both illuminated and non-illuminated areas at about the same rate. This indicates that CO_2 sublimates from ice sources inside the nucleus at a depth that is below the diurnal skin depth. Indeed, CO_2 ice sources very close to the surface would imply a dependence of the flux with the illumination condition, as predicted by comet evolution models (de Sanctis et al. 2005; Marboeuf & Schmitt 2014). The diurnal skin depth has been estimated to ~ 1 cm from MIRO continuum measurements of the subsurface temperature (Schloerb et al. 2015). CO_2 might be present beneath as pure ice or trapped in amorphous water ice or clathrate hydrates (de Sanctis et al. 2005; Marboeuf & Schmitt 2014).

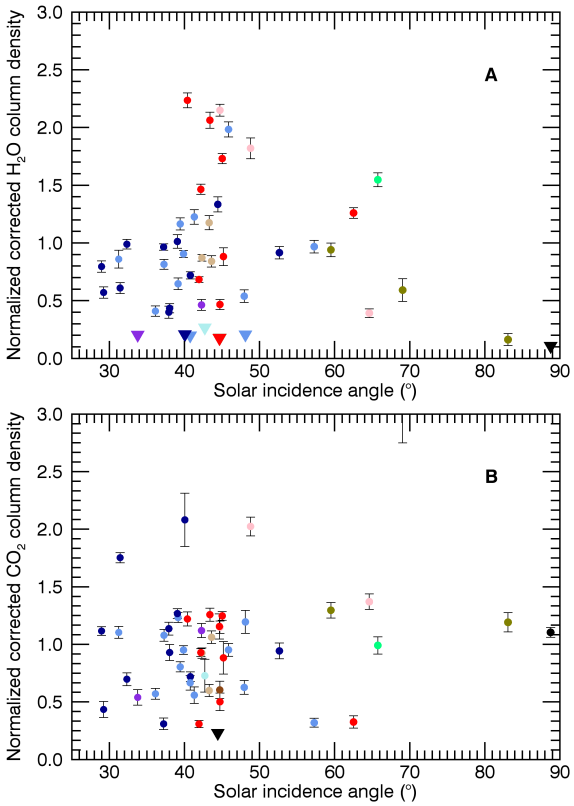

Fig. 9. Column densities corrected from LOS distance and nucleus cross-section as a function of solar incidence angle (see text and Fig. 9). Color coding is that of Fig. 7 and corresponds to regions in P1.

5.2. CO_2/H_2O column density ratio

Column density ratios as a function of solar incidence angle are displayed in Fig. 10A-F, using for each plot cubes for which a specific region is appearing in P1 or P2 (namely, Ash, Babi, Imhotep, Seth, Anuket, and Ma'at, which are the 6 regions the most sampled by the data, Table 4). An increase of the CO_2/H_2O column density ratio with decreasing illumination is observed not only for the top of 67P/C-G body (Imhotep and surroundings, Fig. 10C) but also for regions in the central parts (Seth, Anuket and surroundings, Fig. 10D-E). For LOS above Ma'at (head of 67P/C-G) there is a large scatter in the measured column density ratios (Fig. 10F), likely because these LOS are probing molecules outgassing from other regions under variable illumination conditions.

Table 5 shows for each region the average CO_2/H_2O column density ratios obtained using cubes where the regions are in P1 or in P1&P2 classification. Only data where the solar illumination is high ($i < 50°$) are considered. Within uncertainties, the two options provide the same results. The column density ratio is typically within 0.03 to 0.06. Differences between regions are observed, with values of $\sim$ 0.05 for the top of the body (Imhotep, Ash, Aten) and the top of the head (Hatmehit, Ma'at). On the other hand, lower values $\sim$ 0.03 are measured for LOS above regions in the central parts of the body (Seth) and head (Anuket) which are sampling molecules emitted from near-neck regions. It is worth mentioning that the column density ratio for Hapi in P1 viewed at a mean solar incidence of 67° is also low (0.027 ± 0.002, Table 3). We conclude that the CO_2/H_2O *production rate* ratio from the highly productive neck regions is 0.03 ± 0.01. Overall, there is a

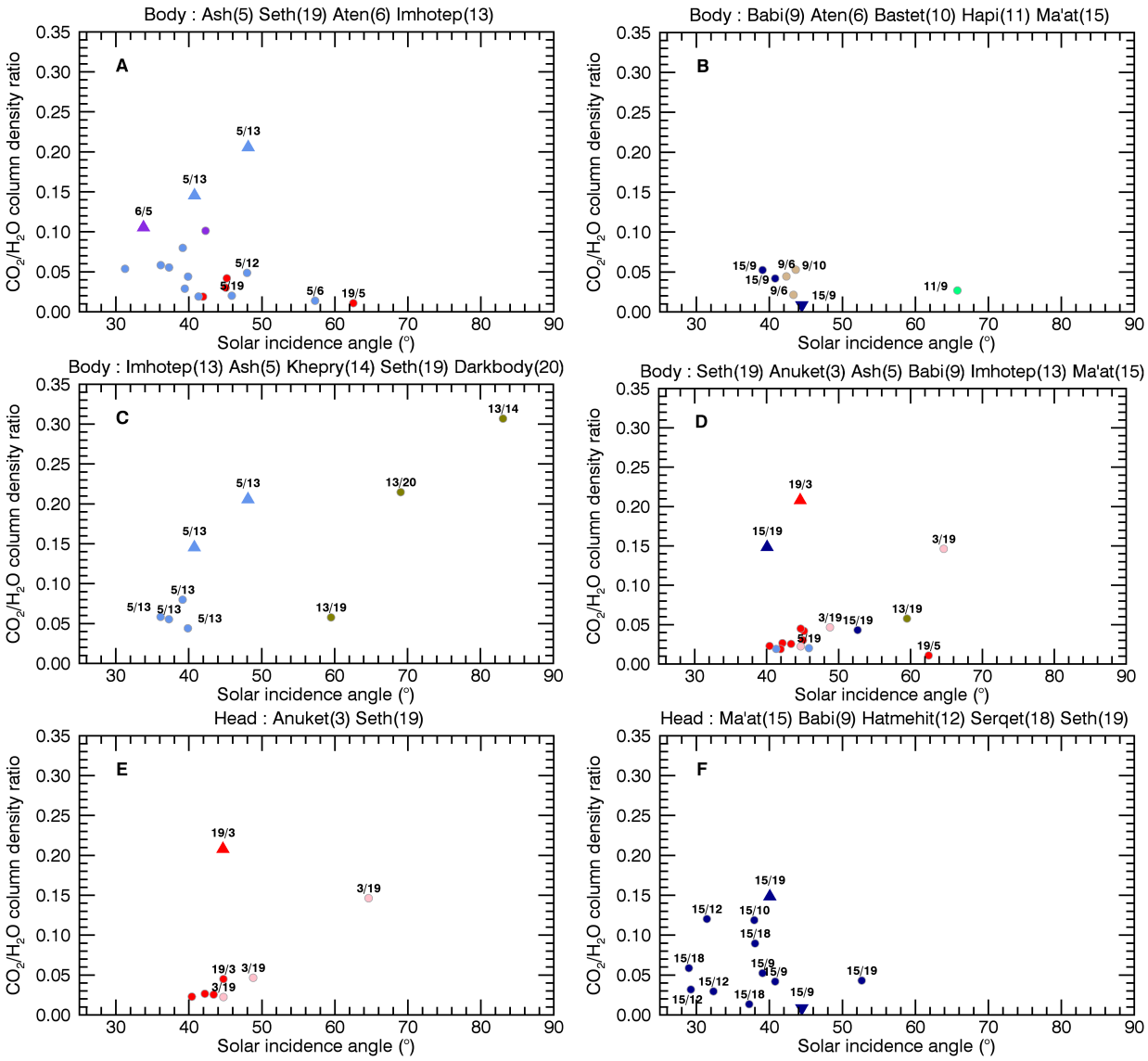

Fig. 10. Column density ratio as function of mean nucleus solar insolation for regions populating the LOS. Limb sounding above Ash (A), Babi (B), Imhotep (C), Seth (D), Anuket (E) and Ma'at (F). Labels given in the plots and titles are those of the regions in P1/P2 (see text). Color coding is that of Fig. 7 and corresponds to regions in P1.

clear trend for higher column density ratios above regions where low H_2O column densities are observed.

The similarity of the CO_2/H_2O column density ratio measured on the body (0.05±0.02 for Ash) and the head (0.06±0.03 on Ma'at), at similar latitudes might suggest that these two units of the nucleus are compositionally similar in terms of CO_2/H_2O *production rate* ratio. However, it needs to be verified that the CO_2/H_2O column density ratio reflects the CO_2/H_2O production rate ratio for these regions. The smaller lobe (head) undergoes daytime surface temperatures higher on average than the larger lobe (body), with the smooth plain Imhotep being even cooler due to the season (grazing sunlight for most of the daytime) (Tosi et al. 2015). So, production rate ratios may not directly translate to abundance ratios inside the nucleus.

For regions sampled at high solar incidence angle (Imhotep region) the CO_2/H_2O column density ratio reaches values as high as 30%. These high values are upper limits to the CO_2/H_2O produc-

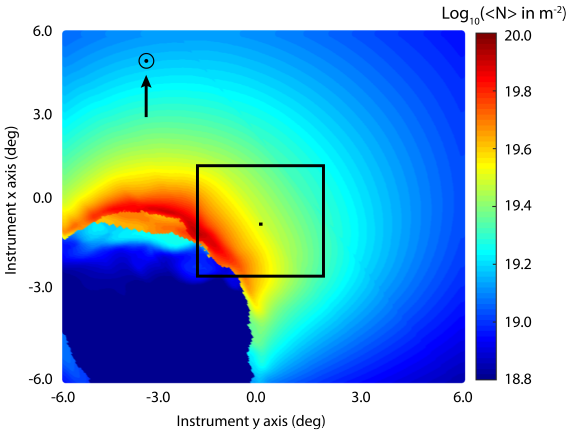

Fig. 11. Decimal log of the modeled water column density on 3 December 2014, 07:01:53 UT (starting time of VIRTIS-H cube 00376211338). The large rectangle is the VIRTIS-M FOV and the small square is VIRTIS-H FOV. The scale of the map is 5.7×5.7 km^2. On the bottom left, the nucleus with the non-illuminated bottom of the "body" (Imothep and Ash) in foreground, and the illuminated "head" in the background. The illuminated Seth and Hapi regions are in between.

tion rate ratio. Indeed, water molecules emitted from illuminated parts of the nucleus (e.g., Hapi) likely contribute to the measured signal. High CO_2/H_2O number density ratios (reaching 200%) were also measured locally (30 km from comet centre) by the ROSINA experiment in September 2014, when the S/C was pointing vertically towards the poorly illuminated Imhotep region (Hässig et al. 2015).

6. Comparison of water columns with gas-dynamics calculations

An interpretation of the retrieved column densities $<N>$ by VIRTIS-H requires the use of a coma model. The relatively low gas production rates at the epoch of the observations imply that to model the physics of the coma of comet 67P/C-G properly necessitates the use of a kinetic approach. The Direct Simulation Monte-Carlo (DSMC) technique is the method of choice to solve the Boltzmann equation in the rarefied atmosphere of comets (Combi 1996).

The Adaptive Mesh Particle Simulator (AMPS) code has been extensively applied to the cometary coma (Tenishev et al. 2008, 2011, Combi et al. 2012, Fougere et al. 2013, Bieler et al. 2015) and has recently been extended to 3D with irregular nucleus shapes (Fougere 2014). In the context of this study, we used AMPS to model the H_2O coma of comet 67P/C-G. Then, we performed calculations of modeled column densities to compare with the VIRTIS-H measurements.

As described in detail by Tenishev et al. (2008) the simulations used surface boundary conditions derived from the thermophysical model of Davidsson and Gutiérrez (2006). The variation of water flux and sublimation temperature were determined by the local solar illumination taking into account the irregular shape of the nucleus (down-sampled version of SHAP5) and self-shadowing. Such a model driven solely by illumination reproduces to a large extent the observations from the ROSINA Comet Pressure Sensor (COPS) as shown in Bieler et al. (2015). Hence, the use of such a model provides a good way to compare the in situ data from ROSINA and the VIRTIS data along the line of sight.

Twelve different cases were performed spanning the 12-h rotation period of the comet nucleus using the geometry on 23 August from 12:00 to 23:00 UT (one case every hour). Bieler et al. show that after accounting for the spacecraft positioning over the next few months that the same model reasonably reproduces the major aspects of the temporal variations of the ROSINA COPS data through December. The column densities were computed at the starting and ending observation times using the reference case with the closest Sun longitude angle to each VIRTIS-H observation time. As an example, Figure 11 illustrates the modeled column densities for observation 00376211338 at its starting time. The VIRTIS-H FOV is shown at the centre of VIRTIS-M FOV.

While the COPS data represents the total gas density, the signal is in fact dominated by the most abundant species, water. Hässig et al. (2015) showed that, even when the comet was at 3.5 AU, the coma of comet 67P/C-G was in general mostly constituted of H_2O. Hence, we multiplied all model column densities by a factor of 0.8 for comparison with the water column densities retrieved from VIRTIS-H. This is the typical water fraction in most comets (Bockelée-Morvan et al. 2004). This assumption ignores the compositional heterogeneities observed by Hässig et al. (2015), which would require a more advanced multi-species coma model.

Figure 12 shows the resulting H_2O averaged modeled column densities of the start and stop times compared with the VIRTIS-H column densities. In Fig. 12B, we decided to ignore the cases when only an upper limit was derived. The error bars for the model are derived from the values of the H_2O column densities at the start and stop times, the differences of which can be large for the extended observations. The model and the data follow each other with a correlation greater than 0.6. In other words, an illumination driven model with a uniformly active but highly irregular surface can reproduce both ROSINA-COPS and VIRTIS-H data, showing general agreement between both instruments regarding both the level and distribution of water vapor in the coma. However, owing to the very large mean free paths for collisions between water molecules in the coma at these low gas production rates and the resulting molecular diffusion close to the nucleus' surface and important kinetic effects, the coma model based on matching the ROSINA-COPS data alone is not sensitive to patchy irregular active regions that are likely distributed around the surface of the nucleus. On the contrary, the VIRTIS-H limb measurements can get as close as a few tens of meters from the nucleus surface revealing these isolated activity regions. This effect may explain most of the differences between the model results and the VIRTIS-H data. Interestingly, the largest discrepancies are observed for high column density values, measured for LOS above Seth and Anuket (respectively, red and pale pink symbols in Fig. 12B), i.e., sampling the water jet above the neck regions. This strengthens the conclusion obtained in Sect. 5, that these regions are more productive in water. An extended analysis of data from VIRTIS-H and other remote sensing instruments will be necessary to get the details of these active regions and improve our understanding of the outgassing of comet 67P/C-G.

In the model, the total water production rate is varying with time. Indeed, the gas fluxes are based on the illumination, which varies with the Sun/nucleus geometry. In these simulations, the

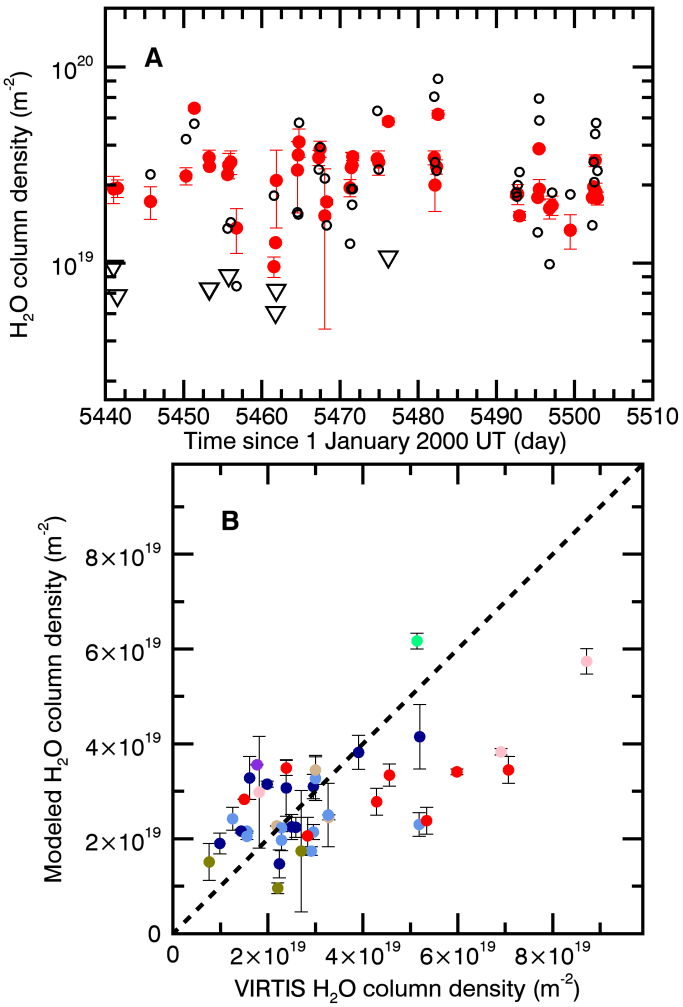

Fig. 12. Column densities from the DSMC model compared to VIRTIS-H column densities. A: Model results (red) and measurements (black) are plotted as a function of time. B: Model as function of measurements, with color coding of Fig. 7 corresponding to regions in P1. Modeled columns have been multiplied by a factor 0.8 to approximate that of H_2O. The markers for the model are at the average point between the values found at the start and stop time of a given observation, which themselves give the error bars. Error bars for VIRTIS-H measurements are shown in Fig. 6.

.

total water production rate ranges from 6.9×10^{25} to 8.7×10^{25} s^{-1} during the 12-h nucleus rotation, which provides a good estimation of comet 67P/C-G activity for the November 2014 to January 2015 period.

7. Conclusion

First observations of the near-nucleus coma of comet 67P/Churyumov-Gerasimenko with the VIRTIS instrument onboard Rosetta have provided interesting information regarding the distribution and levels of production of H_2O, CO_2 and CO at 2.5–2.9 AU from the Sun:

- High water column densities are observed for LOS above neck regions, showing that these regions are the most productive in water vapour.
- The CO_2/H_2O relative production rate from the highly productive neck regions is 3 ± 1%. A 3σ upper limit of 1.8% is measured for the CO/H_2O column density ratio.

- CO_2 is outgassing from both illuminated and non-illuminated regions at about the same rate, indicating that CO_2 sublimates from ice sources inside the nucleus at a depth that is below the diurnal skin depth of $\sim$ 1 cm (Schloerb et al. 2015).
- Gas-dynamics calculations show general agreement between ROSINA and VIRTIS data regarding both the level and distribution of water vapor in the coma. The water production rate in this model ranges from 6.9×10^{25} to 8.7×10^{25} s^{-1} during comet rotation.
- Average rotational temperatures of H_2O and CO_2 are similar ($\sim$ 90–100 K) and consistent with gas-dynamics calculations.

As the comet approaches the Sun, signals will become stronger, allowing us to examine with fine details the outgassing of active regions and diurnal variations, and to detect vibrational bands from minor organics species. We will also be able to monitor the changes of their production rates globally as 67P/C-G approaches perihelion and for different regions, in particular the southern hemisphere as it is progressively illuminated, thus providing important information to understand the source of the volatile molecules inside the nucleus and potentially retrieve their initial composition and possibly spatial heterogeneity.

Acknowledgements. The authors would like to thank the following institutions and agencies, which supported this work: Italian Space Agency (ASI - Italy), Centre National d'Etudes Spatiales (CNES- France), Deutsches Zentrum f́ur Luft- und Raumfahrt (DLR-Germany), National Aeronautic and Space Administration (NASA-USA). VIRTIS was built by a consortium from Italy, France and Germany, under the scientific responsibility of the Istituto di Astrofisica e Planetologia Spaziali of INAF, Rome (IT), which lead also the scientific operations. The VIRTIS instrument development for ESA has been funded and managed by ASI, with contributions from Observatoire de Meudon financed by CNES and from DLR. The instrument industrial prime contractor was former Officine Galileo, now Selex ES (Finmeccanica Group) in Campi Bisenzio, Florence, IT. The authors wish to thank the Rosetta Science Ground Segment and the Rosetta Mission Operations Centre for their fantastic support throughout the early phases of the mission. The VIRTIS calibrated data shall be available through the ESA's Planetary Science Archive (PSA) Web site. With fond memories of Angioletta Coradini, conceiver of the VIRTIS instrument, our leader and friend.

References

Acton, C. H. 1996, Planet. Space Sci., 44, 65

A'Hearn, M. F., Belton, M. J. S., Delamere, W. A., et al. 2005, Science, 310, 258

A'Hearn, M. F., Belton, M. J. S., Delamere, W. A., et al. 2011, Science, 332, 1396

Bieler, A., Fougere, N., Tóth, G., et al., 2015, A&A, submitted

Biver, N. Hofstadter, M. Gulkis, S., et al., 2015, A&A, submitted

Bockelée-Morvan, D. 1987, A&A, 181, 169

Bockelée-Morvan, D., & Crovisier, J. 1989, A&A, 216, 278

Bockelée-Morvan, D., Lis, D. C., Wink, J. E., et al. 2000, A&A, 353, 1101

Bockelée-Morvan, D., Crovisier, J., Mumma, M. J., & Weaver, H. A. 2004, in Comets II, Eds: M.C. Festou, H.U. Keller, and H. Weaver, p391

Bonev, B. P., Mumma, M. J., Villanueva, G. L., et al. 2007, ApJ, 661, L97

Capaccioni, F., Bockelée-Morvan, D., Filacchione, G., et al. 2015a, Lunar and Planerary Science Conference, LPI Contribution No 1832, p. 2494

Capaccioni, F., Coradini, A., Filacchione, G., et al. 2015b, Science, 347, aaa0628

Combes, M., Moroz, V.I., Crovisier, J., et al. 1988, Icarus, 76, 404

Combi, M. R. 1996, Icarus, 123, 207

Combi, M. R., Tenishev, V. M., Rubin, M., et al. 2012, ApJ, 749, 29

Coradini, A., Capaccioni, F., Drossart, P., et al. 2007, Space Sci. Rev., 128, 529

Coradini, A., Capaccioni, F., Erard, S., et al. 2011, Science, 334, 492

Crovisier, J. 1987, A&AS, 68, 223

Crovisier, J., Leech, K., Bockelée-Morvan, D., et al. 1997, Science, 275, 1904

Davidsson, B., & Gutiérrez, P. J. 2006, Icarus, 180, 224

Davidsson, B. J. R., Gulkis, S., Alexander, C., et al. 2010, Icarus, 210, 455

Debout, V., Bockelée-Morvan, D., Zakharov, V. 2015, A&A, in preparation

Dello Russo, N., Mumma, M. J., DiSanti, M. A., et al. 2006, Icarus, 184, 255

de Sanctis, M. C., Capria, M. T., & Coradini, A. 2005, A&A, 444, 605

De Sanctis, M. C., Lasue, J., Capria, M. T., et al. 2010, Icarus, 207, 341

Drossart, P., Semery, A., Bouye, M., et al. 2000, Proc. SPIE, 4131, 78

Fougere, N. 2014, PhD thesis, University of Michigan

Fougere, N., Combi, M. R., Rubin, M., et al. 2013, Icarus, 225, 688

Gulkis, S., and the MIRO Science team, 2014, CBET No 3912

Gulkis, S., Allen, M., von Allmen, P., et al. 2015, Science, 347, aaa0709

Hässig, M., Altwegg, K., Balsiger, H., et al. 2015, Science, 347, aaa0276

Labs, D., & Neckel, H. 1968, ZAp, 69, 1

Lee, S., P. von Allmen, M. Allen, et al. 2015, A&A, submitted

Marboeuf, U., & Schmitt, B. 2014, Icarus, 242, 225

Ootsubo, T., Kawakita, H., Hamada, S., et al. 2012, ApJ, 752, 15

Rothman, L. S., Gordon, I. E., Barbe, A., et al. 2009, J. Quant. Spec. Radiat. Transf., 110, 533

Schloerb, P., Keihm, S., von Allmen, P., et al. 2015, A&A, submitted

Schulz, R. 2012, Planet. Space Sci., 66, 1

Sierks, H., Barbieri, C., Lamy, P. L., et al. 2015, Science, 347, aaa1044

Tenishev, V., Combi, M. R., & Davidsson, B. 2008, ApJ, 685, 659

Tenishev, V., Combi, M. R., & Davidsson, B. 2011, ApJ, 732, 104

Thomas, N., Sierks, H., Barbieri, C., et al. 2015, Science, 347, aaa0440

Tosi, F., Capria, M. T., Capaccioni, F., et al. 2015, Lunar and Planetary Science Conference, 46, 2156

Villanueva, G. L., Mumma, M. J., Bonev, B. P., et al. 2012, J. Quant. Spec. Radiat. Transf., 113, 202

Zakharov, V., Bockelée-Morvan, D., Biver, N., Crovisier, J., & Lecacheux, A. 2007, A&A, 473, 303

List of Objects

Table 3. H_2O and CO_2 band intensities, column densities, and column density ratio.

Obs Id.	H_2O		CO_2		Ratio	Regions[c]
	Band Area[a] (SNR) 10^{-6} (W/m^2/sr)	$< N >$ 10^{19} (m^{-2})	Band Area[b] (SNR) 10^{-6} (W/m^2/sr)	$< N >$ 10^{18} (m^{-2})	$< N_{CO_2} > / < N_{H_2O} >$ (%)	
00375410695	< 1.91	< 0.96	1.28± 0.25 (5.1)	1.22 ± 0.24	> 12.7	12, 16
00375453895	< 1.35	< 0.68	1.04± 0.13 (8.0)	0.99 ± 0.12	> 14.6	16, 12
00375818995	5.76 ± 0.51 (11.4)	2.83 ± 0.25	1.28± 0.20 (6.2)	1.19 ± 0.19	4.2 ± 0.8	19, 5
00376211338	8.92 ± 0.32 (27.5)	4.29 ± 0.16	0.51± 0.08 (6.0)	0.46 ± 0.08	1.1 ± 0.2	19, 5
00376302843	10.70 ± 0.42 (25.7)	5.14 ± 0.20	1.52± 0.12 (13.1)	1.38 ± 0.11	2.7 ± 0.2	11, 9
00376466638	< 1.56	< 0.74	1.19± 0.11 (10.6)	1.08 ± 0.10	> 14.5	5, 13
00376470838	< 1.55	< 0.74	0.86± 0.11 (8.1)	0.78 ± 0.10	> 10.5	6, 5
00376670763	3.20 ± 0.30 (10.6)	1.50 ± 0.14	0.76± 0.11 (6.6)	0.67 ± 0.10	4.5 ± 0.8	19, 3
00376683791	< 1.84	< 0.86	1.99± 0.17 (12.0)	1.77 ± 0.15	> 20.6	5, 13
00376706343	3.45 ± 0.31 (11.1)	1.61 ± 0.15	1.62± 0.12 (13.4)	1.44 ± 0.11	9.0 ± 1.0	15, 18
00376769292	1.64 ± 0.52 (3.1)	0.76 ± 0.24	2.65± 0.18 (14.4)	2.34 ± 0.16	30.7 ± 10.0	13, 14
00377183691	4.84 ± 0.81 (6.0)	2.21 ± 0.37	5.49± 0.52 (10.6)	4.74 ± 0.45	21.5 ± 4.1	13, 20
00377201041	< 1.24	< 0.56	2.46± 0.10 (25.2)	2.13 ± 0.08	> 37.7	21, 10
00377209498	< 1.61	< 0.73	1.76± 0.17 (10.5)	1.52 ± 0.14	> 20.8	19, 3
00377442541	4.04 ± 0.39 (10.4)	1.81 ± 0.17	3.12± 0.16 (20.2)	2.65 ± 0.13	14.6 ± 1.6	3, 19
00377451721	3.95 ± 0.40 (9.9)	1.77 ± 0.18	2.10± 0.12 (18.2)	1.79 ± 0.10	10.1 ± 1.2	6, 5
00377460591	11.60 ± 0.57 (20.4)	5.20 ± 0.25	< 0.51	< 0.43	< 0.8	15, 9
00377678521	6.79 ± 0.23 (30.0)	3.00 ± 0.10	1.59± 0.08 (20.3)	1.33 ± 0.07	4.4 ± 0.3	9, 6
00377693120	8.79 ± 0.26 (33.9)	3.88 ± 0.11	0.62± 0.10 (6.1)	0.52 ± 0.08	1.3 ± 0.2	15, 18
00377746075	6.15 ± 0.38 (16.0)	2.70 ± 0.17	1.86± 0.10 (19.0)	1.56 ± 0.08	5.8 ± 0.5	13, 19
00377766356	3.55 ± 0.36 (9.9)	1.56 ± 0.16	0.91± 0.09 (10.5)	0.76 ± 0.07	4.9 ± 0.7	5, 12
00378023941	2.89 ± 0.31 (9.2)	1.25 ± 0.14	0.89± 0.07 (12.0)	0.73 ± 0.06	5.8 ± 0.8	5, 13
00378037917	5.51 ± 0.24 (23.3)	2.39 ± 0.10	1.22± 0.07 (17.4)	1.00 ± 0.06	4.2 ± 0.3	15, 9
00378047341	4.58 ± 0.39 (11.7)	1.98 ± 0.17	0.77± 0.12 (6.2)	0.63 ± 0.10	3.2 ± 0.6	15, 12
00378053606	5.54 ± 0.20 (27.3)	2.39 ± 0.09	0.55± 0.06 (10.0)	0.45 ± 0.05	1.9 ± 0.2	19, 5
00378326101	14.10 ± 0.36 (39.7)	5.98 ± 0.15	2.24± 0.07 (33.3)	1.80 ± 0.05	3.0 ± 0.1	19, 5
00378340674	7.08 ± 0.63 (11.3)	3.00 ± 0.27	2.00± 0.09 (21.5)	1.61 ± 0.08	5.4 ± 0.5	5, 6
00378446992	< 2.56	< 1.08	2.00± 0.22 (9.0)	1.60 ± 0.18	> 14.8	15, 19
00378954841	17.30 ± 0.58 (29.7)	7.07 ± 0.24	2.33± 0.11 (22.3)	1.80 ± 0.08	2.6 ± 0.1	19, 3
00378963263	8.01 ± 0.45 (17.9)	3.27 ± 0.18	0.58± 0.07 (8.3)	0.45 ± 0.05	1.4 ± 0.2	5, 6
00378981052	7.24 ± 0.46 (15.8)	2.96 ± 0.19	2.24± 0.08 (29.1)	1.74 ± 0.06	5.9 ± 0.4	15, 18
00378996383	21.40 ± 1.06 (20.2)	8.71 ± 0.43	5.25± 0.21 (25.0)	4.05 ± 0.16	4.7 ± 0.3	3, 19
00379861738	5.92 ± 0.30 (19.6)	2.28 ± 0.12	1.74± 0.08 (21.0)	1.27 ± 0.06	5.5 ± 0.4	5, 13
00379870181	5.69 ± 0.34 (17.0)	2.18 ± 0.13	1.57± 0.08 (19.4)	1.15 ± 0.06	5.3 ± 0.4	9, 10
00379877117	6.51 ± 0.27 (23.7)	2.50 ± 0.11	1.01± 0.08 (12.4)	0.74 ± 0.06	3.0 ± 0.3	15, 12
00379896840	7.59 ± 0.39 (19.6)	2.91 ± 0.15	0.76± 0.10 (7.7)	0.56 ± 0.07	1.9 ± 0.3	5, 19
00380098435	3.79 ± 0.29 (13.0)	1.43 ± 0.11	2.40± 0.06 (40.1)	1.72 ± 0.04	12.0 ± 1.0	15, 12
00380112315	18.30 ± 0.44 (41.7)	6.91 ± 0.17	2.16± 0.10 (21.8)	1.55 ± 0.07	2.2 ± 0.1	3, 19
00380115835	14.10 ± 0.41 (34.6)	5.34 ± 0.15	1.70± 0.08 (20.1)	1.22 ± 0.06	2.3 ± 0.1	19, 3
00380228935	2.64 ± 0.35 (7.6)	0.99 ± 0.13	1.65± 0.08 (20.6)	1.18 ± 0.06	11.9 ± 1.7	15, 10
00380257831	6.09 ± 0.20 (30.3)	2.28 ± 0.08	1.41± 0.06 (25.2)	1.00 ± 0.04	4.4 ± 0.2	5, 13
00380459084	6.06 ± 0.35 (17.2)	2.24 ± 0.13	1.38± 0.10 (13.9)	0.97 ± 0.07	4.3 ± 0.4	15, 19
00380701735	4.29 ± 0.33 (12.8)	1.56 ± 0.12	1.81± 0.06 (29.0)	1.24 ± 0.04	8.0 ± 0.7	5, 13
00380717118	9.05 ± 0.47 (19.3)	3.28 ± 0.17	1.02± 0.09 (11.4)	0.70 ± 0.06	2.1 ± 0.2	9, 6
00380723637	7.13 ± 0.42 (17.1)	2.59 ± 0.15	1.96± 0.07 (29.1)	1.36 ± 0.05	5.2 ± 0.4	15, 9
00380733205	12.60 ± 0.37 (33.8)	4.56 ± 0.14	1.76± 0.07 (26.7)	1.21 ± 0.05	2.7 ± 0.1	19, 3
00380743438	14.30 ± 0.47 (30.5)	5.19 ± 0.17	1.51± 0.09 (17.2)	1.04 ± 0.06	2.0 ± 0.1	5, 19
00380758438	8.17 ± 0.37 (22.2)	2.96 ± 0.13	1.24± 0.07 (18.2)	0.85 ± 0.05	2.9 ± 0.2	5, 6

Note : [a] Over 2.60–2.73 μm, to be multiplied by 1.3 for getting the sum of ν_1 and ν_3 band areas; [b] Over 4.230–4.285 μm, to be multiplied by 1.12 for getting the total CO_2 ν_3 band intensity; [c] Labels of the two regions (in P1, P2) which sustain the largest (time averaged) solid angle from the closest LOS point to nucleus centre. Labels are defined in Table 4 and Fig. 7.

Table 4. Stastistics of Nucleus regions sampled by the LOS.

#[a]	Region	N(P1/P2)[b]	#[a]	Region	N(P1/P2)[b]
1	Aker	–	11	Hapi	1/0
2	Anubis	–	12	Hatmehit	1/5
3	Anuket	3/5	13	Imhotep	3/6
4	Apis	–	14	Khepry	0/1
5	Ash	12/6	15	Ma'at	12/0
6	Aten	2/5	16	Maftet	1/1
7	Athor	–	17	Nut	–
8	Atum	–	18	Serqet	0/3
9	Babi	3/4	19	Seth	9/8
10	Bastet	0/3	20-22	un-named	1/1

Notes: [a] Label for referencing the geomorphological regions; [b] Number of cubes for which the regions are contributing in first (P1) and second (P2) position, according to their solid angle as viewed from the point of the LOS at shortest distance to the nucleus centre.

Table 5. CO_2/H_2O column density ratio

#	Region	$< N(CO_2) > / < N(H_2O) >$[a]	
		P1[b]	P1&P2[c]
3	Anuket	0.034 ± 0.012	0.032 ± 0.010
5	Ash	0.045 ± 0.017	0.046 ± 0.020
6	Aten	0.10	0.050 ± 0.022
9	Babi	0.040 ± 0.012	0.043 ± 0.009
12	Hatmehit	–	0.058 ± 0.030
13	Imhotep	–	0.059 ± 0.010
15	Ma'at	0.062 ± 0.028	0.062 ± 0.028
18	Serqet	–	0.054 ± 0.027
19	Seth	0.030 ± 0.008	0.029 ± 0.009

Notes: [a] Cubes where mean solar incidence from LOS is < 50°;
[b] Using cubes where region is contributing in first (P1) position; [c] Using cubes where region is contributing in first (P1) and second position (P2), by its solid angle as viewed from the LOS.